Defective Angiogenesis and Intraretinal Bleeding in Mouse Models With Disrupted Inner Retinal Lamination

Aaron B. Simmons,[1] Morgan M. Merrill,[1] Justin C. Reed,[2] Michael R. Deans,[3,4] Malia M. Edwards,[5] and Peter G. Fuerst[1,2]

[1]University of Idaho, Department of Biological Sciences, Moscow, Idaho, United States
[2]University of Washington School of Medicine, WWAMI Medical Education Program, Moscow, Idaho, United States
[3]University of Utah School of Medicine, Division of Otolaryngology–Head and Neck Surgery, Salt Lake City, Utah, United States
[4]University of Utah School of Medicine, Department of Neurobiology and Anatomy, Salt Lake City, Utah, United States
[5]Johns Hopkins University School of Medicine, Wilmer Eye Institute, Baltimore, Maryland, United States

Correspondence: Peter G. Fuerst, Department of Biological Sciences, University of Washington WWAMI Medical Education Program, University of Idaho, Moscow, ID 83844, USA;
fuerst@uidaho.edu.

Submitted: October 13, 2015
Accepted: January 31, 2016

Citation: Simmons AB, Merrill MM, Reed JC, Deans MR, Edwards MM, Fuerst PG. Defective angiogenesis and intraretinal bleeding in mouse models with disrupted inner retinal lamination. *Invest Ophthalmol Vis Sci*. 2016;57:1563–1577. DOI:10.1167/iovs.15-18395

Purpose. Abnormal retinal angiogenesis leads to visual impairment and blindness. Understanding how retinal vessels develop normally has dramatically improved treatments for people with retinal vasculopathies, but additional information about development is required. Abnormal neuron patterning in the outer retina has been shown to result in abnormal vessel development and blindness, for example, in people and mouse models with *Crumbs homologue 1* (*CRB1*) mutations. In this study, we report and characterize a mouse model of inner retinal lamination disruption and bleeding, the Down syndrome cell adhesion molecule (*Dscam*) mutant, and test how neuron-neurite placement within the inner retina guides development of intraretinal vessels.

Methods. *Bax* mutant mice (increased neuron cell number), *Dscam* mutant mice (increased neuron cell number, disorganized lamination), *Fat3* mutant mice (disorganized neuron lamination), and *Dscam* gain-of-function mice ($Dscam^{GOF}$) (decreased neuron cell number) were used to manipulate neuron placement and number. Immunohistochemistry was used to assay organization of blood vessels, glia, and neurons. In situ hybridization was used to map the expression of angiogenic factors.

Results. Significant changes in the organization of vessels within mutant retinas were found. Displaced neurons and microglia were associated with the attraction of vessels. Using *Fat3* mutant and $Dscam^{GOF}$ retinas, we provide experimental evidence that vessel branching is induced at the neuron-neurite interface, but that other factors are required for full plexus layer formation. We further demonstrate that the displacement of neurons results in the mislocalization of angiogenic factors.

Conclusions. Inner retina neuron lamination is required for development of intraretinal vessels.

Keywords: neovascularization, retinal vasculature, microglia, Müller glia, astrocytes

Retinal neurons in humans are nourished by three vasculature networks, or plexi, and the choroidal vessels, an organization that is shared between human and mouse.[1] Many blinding diseases, including macular degeneration, vasculopathy of prematurity, and diabetic retinopathy, are caused by aberrant growth and maintenance of these vessels, resulting in retinal neuron death and subsequent vision loss.[2–4] Understanding the normal development of these vessels will help us better understand what happens to them during these disease processes.

The mouse retina serves as an excellent model for understanding basic principles guiding vessel development because its development and structure is similar to the human retina.[1] The immature retina is nourished by a fetal or hyaloid vascular system, which resides within the vitreous and is eventually replaced by retinal vessels during development.[1] Hyaloid vessels begin to regress at birth in the mouse, as the retinal vessels enter the retina through the optic nerve head (ONH). Retinal vessels proliferate out radially across the surface of the retina to form the superficial plexus (SP), complete by postnatal day 7 (P7). The retinal vessels then dive to the outer plexiform layer (OPL) to form the deep plexus (DP), complete by P14, and ascend back to the inner plexiform layer (IPL) to form the intermediate plexus (IP), complete by P21.[1]

The retinal vasculature develops in response to a complex series of molecular and cellular interactions among the retina's neurons, glia, and vascular cells. Retinal neurons have been shown to direct vessel growth through the release and/or regulation of proangiogenic factors, such as VEGF,[5–8] antiangiogenic factors, such as semaphorins,[9,10] and through interactions with glia.[11] The retina contains three populations of glia that are important for development and maintenance of the retinal vasculature: Müller cells (MCs), astrocytes and microglia. Müller cells are derived from retinal progenitors and are the last population of cells to be born within the retina.[12] During development, MCs release VEGF in response to neural-induced hypoxia[13] and are thought to provide scaffolding along which endothelial cells migrate during development.[1] Mature MCs

Investigative Ophthalmology & Visual Science

project radial processes spanning the retina, forming the outer and inner limiting membranes. Tangential MC processes wrap blood vessels to help make up the blood-retina-barrier (BRB), and also play a role at neural synapses.[14] Astrocytes and microglia migrate into the retina through the ONH during development.[15,16] On entry, astrocytes proliferate and migrate centrifugally across the laminin-rich surface of the retina and provide a template directing the migration of endothelial cells in mice.[17,18] After development, astrocytes serve to stabilize vessels through the release of VEGF[19] and wrap superficial vessels to help make up the BRB.[11] Microglia promote branching of superficial vessels during development and are thought to play a role in directing vessel growth into the retina.[16] The initial invasion and subsequent formation of the superficial vessels has been well studied; however, much less is known about mechanisms responsible for attracting and organizing the intraretinal vessels forming the deep and intermediate plexi.

In this study, we test the role of neuron placement on intraretinal vascular development by using mouse models in which neuron placement within the inner retina is disrupted. Retinal neurons are organized in three cellular layers: the outer nuclear layer (ONL), inner nuclear layer (INL), and retinal ganglion cell layer (RGL); and two synaptic layers: the OPL and IPL, all of which are notable for their stereotypic organization into alternating laminae.[20,21] Disorganization of ONL lamination and vascular defects has been documented in humans and mice carrying *Crumbs1* mutations.[22] Similarly, we report abnormal angiogenesis and intraretinal bleeding associated with laminar disruption within the inner retina.

In this study, we find significant differences in the organization of blood vessels in retinas with ectopic neurons within the IPL (*Bax* mutants) and in those with highly disrupted neuron patterning within the inner retina (*Dscam* mutants). The latter also exhibit frequent intraretinal bleeding. Using *Fat3* mutant mice, which contain an additional plexiform lamina, and using *Dscam* gain-of-function ($Dscam^{GOF}$) mice, in which vessel branching occurs at the INL/IPL interface yet lack an IP, we provide experimental evidence that vessel branching occurs at the neuron-neurite interface. Next, we tested the relative contribution of glial organization and neuron misplacement to vessel organization defects. Glial organization was largely maintained in retinas with misplaced neurons. The displacement of neurons in the *Dscam* mutant retina results in the ectopic expression and localization of angiogenic factors suggesting a mechanism by which displaced neurons could deflect growing vessels, resulting in fragile growing vessels and intraretinal bleeding.

Materials and Methods

Mouse Strains and Handling

Mice were handled in accordance with protocols approved by the Animal Care and Use Committees at the University of Idaho and the University of Utah and with the ARVO Statement for the Use of Animals in Ophthalmic and Vision Research. $Dscam^{-/-}$ mice: the $Dscam^{2J}$ (stock number: 006038; The Jackson Laboratory, Bar Harbor, ME, USA)[23] and *Dscam* FD[24] loss-of-function alleles were used in this study. $Dscam^{GOF}$ mice were previously generated[25] and are available through The Jackson Laboratory (stock number: 025543). *Bax* mutant mice were obtained from The Jackson Laboratory (stock number: 002994) and *Fat3* mutant retinas were provided by Michael Deans (University of Utah).[26]

Immunohistochemistry

Tissues were prepared as previously described.[25]

Antibodies and Stains

Primary antibodies included mouse anti-glutamine synthetase (GS) (MAB302, 1:1000; Millipore, Darmstadt, Germany), mouse anti-glial fibrillary acidic protein (GFAP) (3670, 1:200; Cell Signaling Technology, Danvers, MA, USA), rabbit anti-GFAP (Z0334, 1:500; Dako, Carpinteria, CA, USA), rabbit anti-IBA-1 (019-19741, 1:500; Wako, Richmond, VA, USA), rabbit anti-VEGF (A20, 1:200; Santa Cruz Biotechnology, Santa Cruz, CA, USA), mouse anti-PAX6 (1:500; developed by Kawakami, Developmental Studies Hybridoma Iowa City, IA, USA), and rabbit anti-Vimentin (ab45939, 1:300; ABCAM, Cambridge, MA, USA). Secondary antibodies were used at 1:500 room temperature (RT) or 1:1000 4°C overnight (Jackson ImmunoResearch, West Grove, PA, USA). Stains included Isolectin GS-B4 Alexa 568 (I21412, 1:200; Invitrogen, Grand Island, NY, USA), 4′,6-diamidino-2-phenylindole (DAPI) (4083, 1:50,000 from 1 mg/mL stock; Cell Signaling Technology), DRAQ5 (62251, 1:2000; Thermo Scientific, Waltham, MA, USA).

Microscopy

Micrographs were captured from a Nikon (Melville, NY, USA) or Olympus (Center Valley, PA, USA) spinning disk confocal microscope, an Olympus Fluoview scanning laser confocal microscope, a Leica Stereoscope (Buffalo Grove, IL, USA), or Leica DMR microscope. Adobe Photoshop (Adobe Systems, Inc., San Jose, CA, USA) and FIJI (National Institutes of Health, Bethesda, MD, USA) were used to process images. Any modifications to the brightness or contrast of images were performed uniformly across the image, in accordance with journal policies.

Cell Counts

For neurons, thickness of the cellular layers was quantified as previously described.[25] Density of MCs was quantified in sections stained with DAPI and GS. Numbers were normalized per unit length of retina. Density of microglia was quantified in whole retinas stained with ionized calcium-binding adapter molecule 1 (IBA-1, Wako Chemicals USA, Inc., Richmond, VA, USA). Images were captured through the entire retina at 1-μm increments along the *z*-axis and were then split into microglia found in the IPL or OPL based on physical separation of cell bodies. These counts were normalized per unit volume in the IPL and per unit area in the OPL. In all counts, the peripheral and central retina were sampled equally and were quantified at P28.

Vessel Density

Vessel density was quantified in P28 whole retinas stained with GS isolectin. Images were captured through the entire retinal vessels at 1-μm increments along the *z*-axis. Twelve images were captured from each retina (four central, four mid, and four peripheral). Image stacks were imported into FIJI and were traced with the plugin, Simple Neurite Tracer.[27] For each image stack, the total length of vessels was normalized per unit volume.

Plexus and Astrocyte Coverage

The P28 whole retinas stained with GS isolectin or GFAP were imaged and sampled at 1 μm along the *z*-axis. Eight images were captured from each retina (four central and four peripheral). Image stacks were then imported into FIJI and *z*-projections were generated. Vessels found within the IPL of $Bax^{-/-}$ and the INL of $Fat3^{-/-}$ retinas were not included in the analysis. The IP data for $Dscam^{-/-}$ and $Dscam^{GOF}$ retinas includes everything between the SP and DP. The percent coverage was then measured in FIJI from the *z*-projection images.

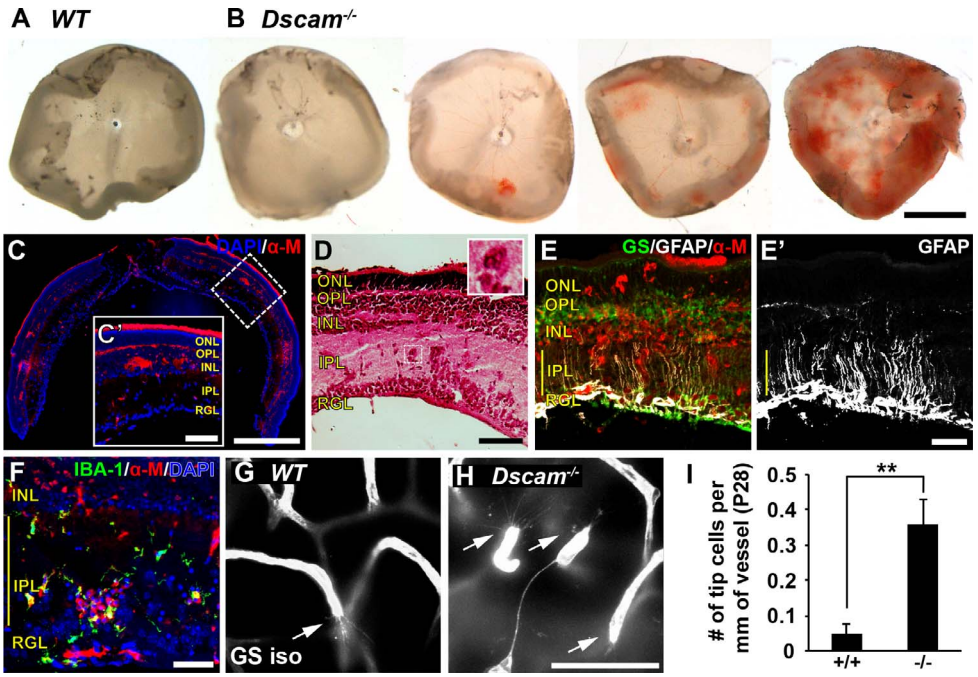

Figure 1. Retinal bleeding and glial activation in *Dscam*$^{-/-}$ mice. Retinal bleeding was observed in 52% of *Dscam*$^{-/-}$ retinas between P16 and P20 ($n = 23$). (**A**) *WT* retina, no retinal bleeding. (**B**) *Dscam*$^{-/-}$ retina, varying amounts of retinal bleeding from none to severe. (**C**) Cross section of bloody *Dscam*$^{-/-}$ retina stained with DAPI and α-mouse to visualize locations of bleeding. Retinal bleeding is found within the inner retina. (**C'**) *Zoomed-in insert* of cross section. (**D**) Cross section of bloody *Dscam*$^{-/-}$ retina stained with hematoxylin and eosin. Red blood cells can be seen within the retina outside of blood vessels. *Inset* shows higher magnification of a clump of red blood cells found within the IPL. (**E**) Cross section of bloody retina stained with GS, GFAP, and α-mouse. (**E'**) The GFAP split out for better visualization; GFAP can be seen throughout MC processes within bloody spots. (**F**) Cross section of retina stained with DAPI, IBA-1, and α-mouse. Microglia can be seen in locations in which retina is bloody. (**G**, **H**) Images of endothelial tip cells in *WT* and *Dscam*$^{-/-}$ retinas at P28. (**I**) *Graph* illustrating density of tip cells at P28. Very few tip cells were observed in *WT* retinas. Significantly more tip cells were found within *Dscam*$^{-/-}$ retinas. *Error bars*: SD. Student's *t*-test was used to analyze data. $^{**}P < 0.002$. Abbreviations: α-M, anti-mouse; GS iso, GS isolectin. *Scale bars*: (**B**) 1 mm, (**C**) 500 μm, (**C'**) 100 μm, (**D**) 100 μm, (**E'**) 50 μm, (**H**) 50 μm. (**D**, *inset*), 40 × 40 μm.

Blood Vessel and MC Radial Process Orientation

The P28 retina sections stained with DAPI and GS isolectin or GS were imaged and imported into FIJI, where the orientation within the IPL was measured with respect to the nerve fiber layer (NFL). Each recorded orientation was classified as one observation and the data were converted to the percentage of observations at a particular angle in 10° increments.

Blood Vessel Branch Points (BPs)

The P28 retina sections stained with DAPI and GS isolectin were imaged and imported into FIJI. All BPs within a section were identified and recorded based on location within the different laminae of the retina. The IPL was further divided into S1 to S5, according to convention established by Ramon y Cajal.[28] Branch points found within S1 were considered to be found within the IP; BPs found in S2 to S5 were considered to be found within the IPL. The data were then converted to the percentage of BPs found within the different laminae for a given retina section.

Nuclei to Nearest Vessel Measurement

The P14 *Dscam*$^{-/-}$ whole retinas stained with DRAQ5, GS isolectin, and IBA-1 were imaged on a confocal microscope and imported into Bitplane's Imaris (Bitplane USA, Concord, MA, USA). Images were sampled equally from the peripheral and central retina to capture two developmental time-points. Within Imaris, the images were digitally reconstructed as surfaces and spots for the vessels and nuclei, respectively. Spots within the IPL were then isolated and classified. Endothelial nuclei were identified by their elongated shape and their location within GS isolectin, microglia by IBA-1, and the remainder were classified as neurons. The distance transformation function was then used to measure the closest surface (blood vessel) to each of the spots (nuclei) within the IPL. As a randomized control, blood vessels were flipped along the horizontal axis to randomize the location of nuclei and the measurements were repeated. Spots encapsulated by vessels in the flipped control were excluded from the analysis.

Protein Extraction and Western Blot

Protein was extracted from P14 retinas from *Dscam* mutants and wild-type littermate controls using mem-PER Eukaryotic Protein Extraction Reagent Kit (Thermo Scientific, Rockford, IL, USA); 20 μg total protein was loaded into each lane and was separated using 10% acrylamide gel. Blots were transferred to polyvinylidene difluoride (PVDF) membranes (162-0174; Bio-Rad Laboratories, Hercules, CA, USA) and blocked in tris-buffered saline and tween 20 (TBST) (0.05% Tween) and 3% nonfat dry milk. Blots were probed with rabbit anti-VEGF antibody (1:1000; Santa Cruz Biotechnology) for 75 minutes at RT followed by four 5-minute washes in TBST at RT. Anti-VEGF was detected using goat anti-rabbit horseradish peroxidase (HRP)-linked antibody (7074, 1:25,000; Cell Signaling Technology), diluted in 3% milk. Blots were then washed four times for 5 minutes in TBST at RT. Immoblin Western Chemiluminescent HRP Substrate Kit (Millipore) was used to detect antibodies. Blots were then striped and re-probed with rabbit anti-Glyceraldehyde-3-Phosphate Dehydrogenase (anti-GAPDH) antibody (247002, 1:1000; Synaptic Systems, Goettingen, Germany)

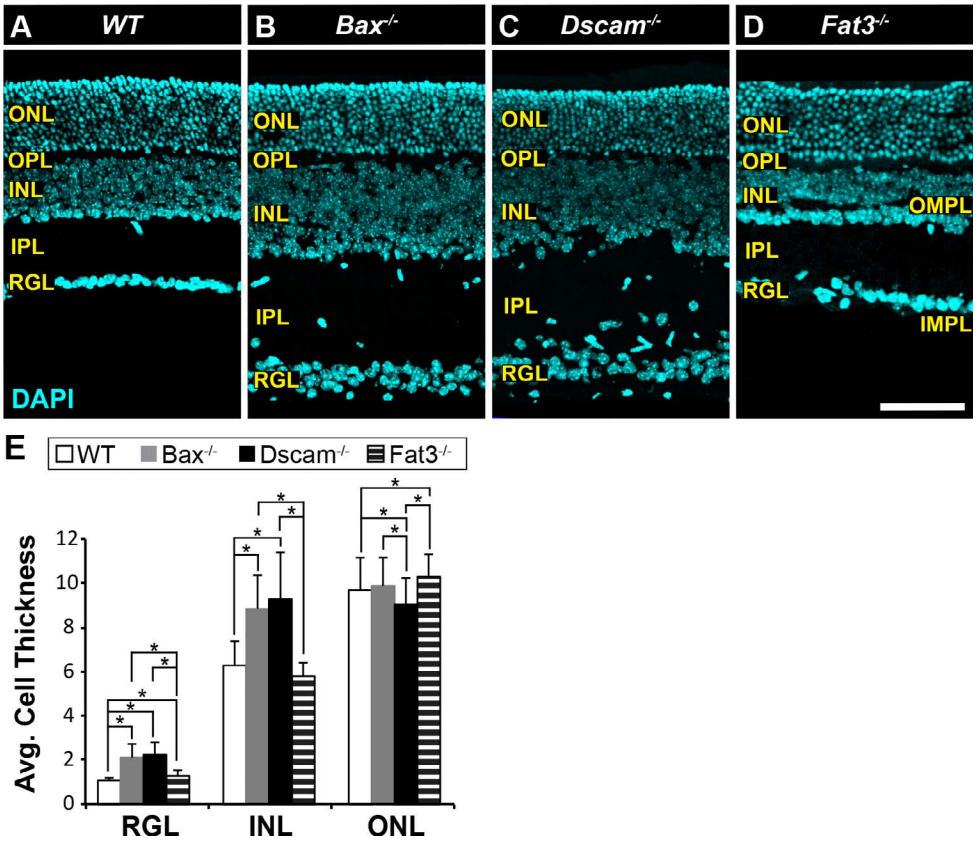

Figure 2. Mutant mouse strains used in this study. (**A–D**) Postnatal day 28 retina sections stained with DAPI. (**A**) *WT* retina. The stereotypic organization of the retina consists of three cellular laminae: ONL, INL, and RGL, separated by two plexiform layers: OPL and IPL. (**B**) *Bax*$^{-/-}$ retina. Increased thickness in the INL, IPL, and RGL due to a defect in developmental cell death. Lamination of the neural retina is maintained, except ectopic neural somas located in IPL. (**C**) *Dscam*$^{-/-}$ retina. Increased thickness in the INL, IPL, and RGL due to a defect in developmental cell death. Lamination of the outer retina is maintained while the inner retina (INL, IPL, and RGL) is highly disrupted. (**D**) *Fat3*$^{-/-}$ retina. Cellularity is maintained. Abnormal migration of neurons results in more cells found within the RGL and fewer in the INL. Two ectopic plexiform layers form. One in the INL and the other below the RGL, termed the OMPL and IMPL, respectively. (**E**) Cell thickness of each nuclear layer quantified; $n \geq 3$ mice were used for each strain. *Error bars*: SD. A 1-way ANOVA was used to statistically analyze data for each cellular layer separately (RGL: $P \leq 6.61 \times 10^{-52}$; INL: $P \leq 1.45 \times 10^{-44}$; ONL: $P \leq 7.31 \times 10^{-5}$). Tukey's pairwise comparison was used to compare each group. *Denotes statistical differences between groups. *Scale bar*: (**D**) 100 μm.

and detected with anti-rabbit HRP linked antibody (Cell Signaling Technology). Steps for anti-GAPDH were performed identical to anti-VEGF. Densitometry was performed using FIJI to calculate the relative densities between anti-VEGF and anti-GAPDH.

In Situ Hybridization

Probes were generated as previously described[29] with the following modifications. Primers to make to make probe templates: *Vegfa* forward (TGTCTACCAGCGAAGCTACT), *Vegfa* reverse (TCGTTTAACTCAAGCTGCCT), *Vegfr2* forward (ATTCAGAGCGATGTGTGGTC), *Vegfr2* reverse (GTCT GTCTGGCTGTCATCTG), *Sema3C* forward (ATCGGCAGTGT GTGTGTATC), *Sema3C* reverse (GAACCTAGAGCAAGAGT GGC), *Sema3E* forward (GGCAAGTATGGAACCACCAA), *Sema3E* reverse (CTGGAGCAGGATATGCCATC). In vitro transcription mixture was composed of 1 μg cDNA, 4 μL 10× T7 or SP6 buffer (Roche, Pleasanton, CA, USA), 4 μL T7 or SP6 RNA polymerase (Roche), 1 μL RNase inhibitor (Roche), 4 μL digoxigenin or fluorescein deoxyribose nucleotide triphosphates (dNTPs) (Roche) and RNase free water to 40 μL. Samples were incubated at 37°C overnight and 4 μL LiCl, 4 μL ethylenediaminetetraacetic acid (EDTA), and 150 μL EtOH was added to the samples. RNA was chilled at −80°C and resuspended in 20 μL RNase free water.

Tissues for hybridization were prepared by fixing P14 from *Dscam* mutant and wild-type littermate enucleated and hemisected eyes (cornea and lens removed) in 4% paraformaldehyde with 5% sucrose at RT for 30 minutes. Retinas were then dissected out of the eye cup and washed three times for 10 minutes in phosphate buffer with 5% sucrose. Tissues were cryopreserved by equilibrating them in 30% sucrose and then embedded and frozen down in a 2:1 mixture of optimal cutting temperature compound (OCT, Sakura Finetek USA, Inc., Torrance, CA, USA): 30% sucrose. Tissues were sectioned at 6 μm using a cryostat and were placed onto charged slides. Slides were then dried overnight in a desiccator at RT. Hybridization was prepared as previously described.[30,31]

Results

Blood Leakage in Developing Dscam Mutant Retinas

A varying degree of intraretinal bleeding was observed within 52% of developing retinas in mice lacking *Dscam* (*Dscam*$^{-/-}$) between P16 and P20 (Figs. 1A, 1B), a time point when intraretinal vessels are forming.[1] Histologic staining of *Dscam*$^{-/-}$

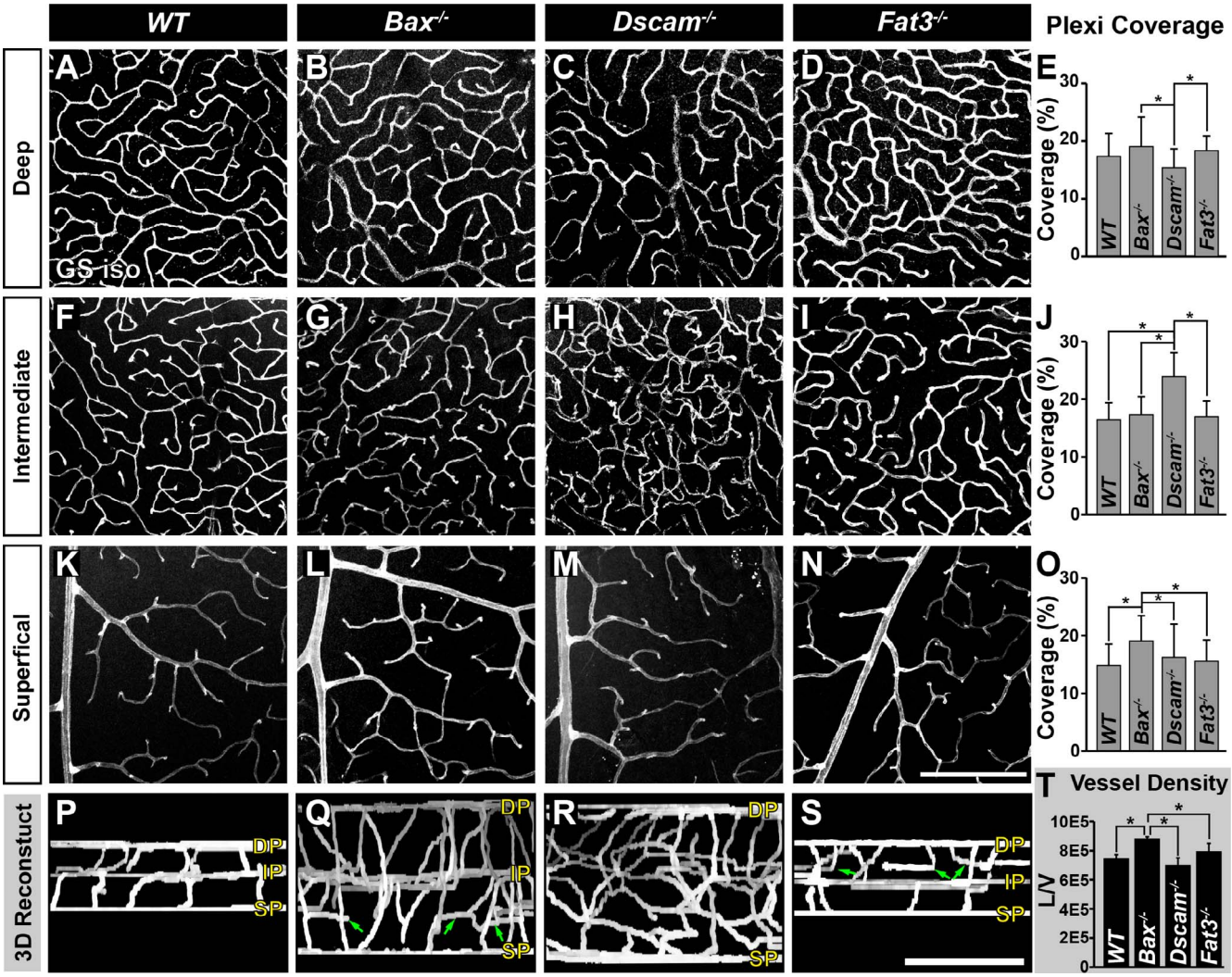

Figure 3. Analysis of neural organization and density on formation of vascular plexi. Postnatal day 28 whole retinas stained with GS isolectin. (**A–E**) Analysis of the DP. A significant decrease in vascular coverage was detected in *Dscam*$^{-/-}$ retinas, compared with *Bax*$^{-/-}$ and *Fat3*$^{-/-}$. (**F–J**) Analysis of the IP. *Dscam*$^{-/-}$ retinas lack a defined IP, data are representative of all vessels between the SP and DP. (**K–O**) Analysis of the SP. A significant increase in vascular coverage was detected in *Bax*$^{-/-}$ retinas. (**P–S**) Digital reconstruction of vessel image in whole mount flipped to view the *x/z*-axis. Ectopic vessels are found throughout the IPL of *Bax*$^{-/-}$ and the INL of *Fat3*$^{-/-}$ retinas (*green arrows*). (**T**) Graph representing total vessel density; $n \geq 3$ mice was used for each strain per quantification. *Error bars*: SD. A 1-way ANOVA was used to statistically analyze all data separately (DP coverage: $P \leq 6.94 \times 10^{-18}$; IP coverage: $P = 0.00$; SP coverage: $P \leq 2.80 \times 10^{-5}$; vessel density: $P \leq 1.95 \times 10^{-3}$). Tukey's pairwise comparison was used to compare each group. *Denotes statistical differences between groups. *Scale bars*: (**N**) 200 μm, (**S**) 100 μm.

retinas revealed that this bleeding occurred within the inner retina (Figs. 1C, 1D). Upregulation of GFAP was observed within MCs within the bloody patches (Figs. 1E, 1E'), as well as an infiltration of IBA-1 positive microglia (Fig. 1F). Intraretinal bleeding was observed in mice in which the *Dscam* gene was conditionally targeted in the retina with *Pax6α-Cre*, indicating that this phenotype was not secondary to hydrocephalus that occurs in *Dscam* mutants[32] (Supplementary Fig. S1). Intraretinal bleeding was not observed in adult *Dscam* mutants (age >P35), indicating that the integrity of the vascular network was eventually established in these mice. Consistent with this, a significant increase in blood vessel growth cones was detected at P28 in *Dscam*$^{-/-}$ mice, a time point when angiogenesis is largely complete in the wild-type (*WT*) retina (Figs. 1G–I).

Dscam is not expressed by cells of the vasculature or glia,[33] but rather is required for neuron patterning and developmental cell death within retinal neurons.[29] Because the neural retina begins to develop before vessels invade the inner retina, we hypothesized that cues from the neural retina or glia act to provide guideposts that are used by developing blood vessels and that abnormalities in retinal lamination could potentially drive the observed vascular pathology.

Genetic Approach to Vary Neuron Placement

Mouse mutants in which neuron number and lamination are disrupted were assembled to test the hypothesis that neurons facilitate blood vessel organization. The *Bax* mutant retina (*Bax*$^{-/-}$) has an increase in cell number and misplacement of neurons in the IPL as a result of a defect in developmental cell death (Fig. 2B). Neuron cell number in the *Bax*$^{-/-}$ mutant retina is similar to that observed in *Dscam*$^{-/-}$ retina (Fig. 2C), the latter of which also features uneven INL lamination.[25,34] Cell number is similar to the *WT* in the *Fat3* mutant retina (*Fat3*$^{-/-}$); however, ectopic plexiform laminae form within the INL and just below the RGL in *Fat3*$^{-/-}$ retinas, termed the outer and inner misplaced plexiform layer (OMPL and IMPL), respectively (Fig. 2D).[26] Some neurons normally found within

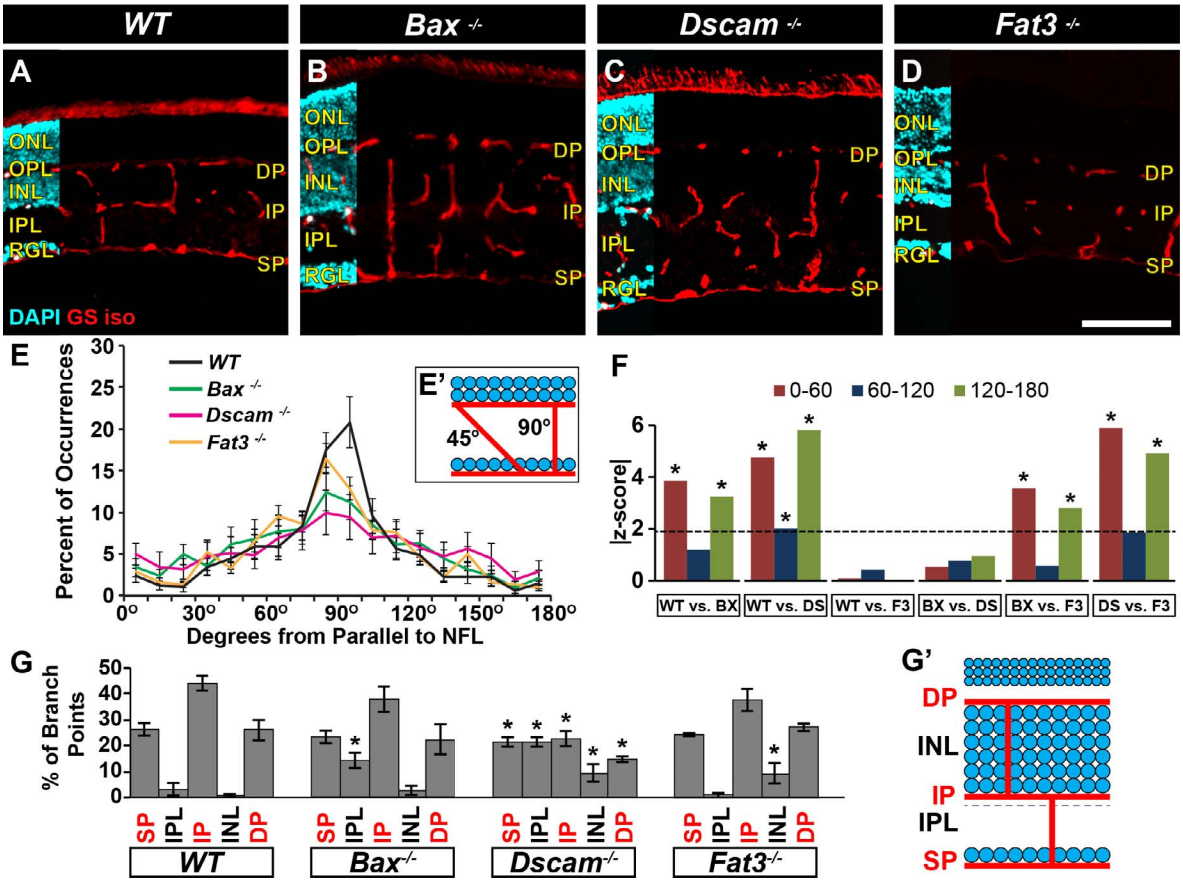

Figure 4. Analysis of neural organization and density on interplexus connections. (**A**–**D**) Postnatal day 28 retina sections stained with GS isolectin and DAPI. (**E**) The trajectory of vessels was quantified throughout the IPL. Most vessels in *WT* and *Fat3*$^{-/-}$ ran perpendicular to the NFL. *Bax*$^{-/-}$ vessels mainly ran perpendicular to the NFL with some ectopic vessels running parallel. *Dscam*$^{-/-}$ vessels were much more tortuous. *Error bars*: SD. (**F**) Mann-Whitney *U* tests were used to statistically analyze orientation data. The data were grouped in increments of 30°. *Graph* represents the absolute *z*-score value generated by test. *Dotted line* represents the threshold a value must pass to be considered statistically different. *Denotes that threshold was met. (**G**) Branching locations were analyzed for interplexus vessels. Vessels within the *WT* branch at areas corresponding to vascular plexi. A significant increase in BPs was observed in the IPL of *Bax*$^{-/-}$ and the INL of *Fat3*$^{-/-}$. Branch points were uniformly distributed across *Dscam*$^{-/-}$ retinas. *Error bars*: SD. Student's *t*-test was used to statistically analyze *WT* versus other genotypes. Percent data were converted to arcsine for analysis. *$P \leq 0.05$; $n \geq 3$ mice was used for each strain per quantification. BX, *Bax*$^{-/-}$; DS, *Dscam*$^{-/-}$; F3, *Fat3*$^{-/-}$. *Scale bar*: (**D**) 100 μm.

the INL are mislocalized to the RGL.[26] Quantification of cell numbers was consistent with previous publications (Fig. 2E).[25,26,34]

Vessel Disorganization Correlates With Laminar (Dis)Organization

The adult retinal vasculature consists of three capillary networks, or plexi: the SP, IP, and DP. We measured if the formation of these plexi was normal across these mutant strains at an age when their development is complete, P28 (Fig. 3). The DP develops normally in the *Bax*$^{-/-}$ and *Fat3*$^{-/-}$ retinas. *Dscam*$^{-/-}$ retinas have significantly reduced DP coverage compared with *Bax*$^{-/-}$ and *Fat3*$^{-/-}$ retinas (Figs. 3A–E, 3P–S). Formation of the IP was normal within *Bax*$^{-/-}$ and *Fat3*$^{-/-}$ retinas, compared with *WT* (Figs. 3F, 3G, 3I, 3J, 3P, 3Q, 3S). *Dscam*$^{-/-}$ retinas lacked a defined IP (Figs. 3H, 3J, 3R). Although the SP was normal within all of the models, vessel coverage was significantly increased in the *Bax*$^{-/-}$ retina compared with all strains (Figs. 3K–O, 3P–S). Additionally, ectopic vessels were observed running parallel to the plexi within *Bax*$^{-/-}$ and *Fat3*$^{-/-}$ retinas in areas correlated to the IPL and OMPL, respectively (Figs. 3Q, 3S, arrows).

We next asked whether the total density of vessels reflected the neural densities within the different strains. Calculation of vessel densities revealed a significant increase in vessel density in *Bax*$^{-/-}$ retinas compared with all other strains (Fig. 3T).

The interplexus vessels connecting the three plexi were then analyzed (Figs. 3P–S, Figs. 4A–F). Measuring the trajectory these vessels took when traveling through the retina demonstrated that most vessels projected perpendicular within *WT* and *Fat3*$^{-/-}$ retinas (Figs. 4A, 4D–F). Vessels in *Bax*$^{-/-}$ retinas followed a similar trend except that statistically more vessels within the IPL were found running parallel to the retinal laminae, when compared with *WT* and *Fat3*$^{-/-}$ retinas (Figs. 4B, 4E, 4F). Vessels within *Dscam*$^{-/-}$ retinas followed a more tortuous trajectory with statistically less perpendicular vessels and statistically more running between 0 and 60° and 120 and 180°, when compared with *WT* and *Fat3*$^{-/-}$ retinas (Figs. 4C, 4E, 4F). No statistical differences were detected between *Bax*$^{-/-}$ and *Dscam*$^{-/-}$ retinas. This is probably due to how the data was lumped together in increments of 60° for statistical analysis. Interplexus branching was also examined (Fig. 4G). Most vessel BPs within *WT* retinas occurred at locations spatially correlated to the three vascular plexi (Fig. 4G). A significant increase in BPs was detected within the IPL of *Bax*$^{-/-}$ retinas (Fig. 4G). The BPs within *Dscam*$^{-/-}$ retinas were distributed uniformly throughout

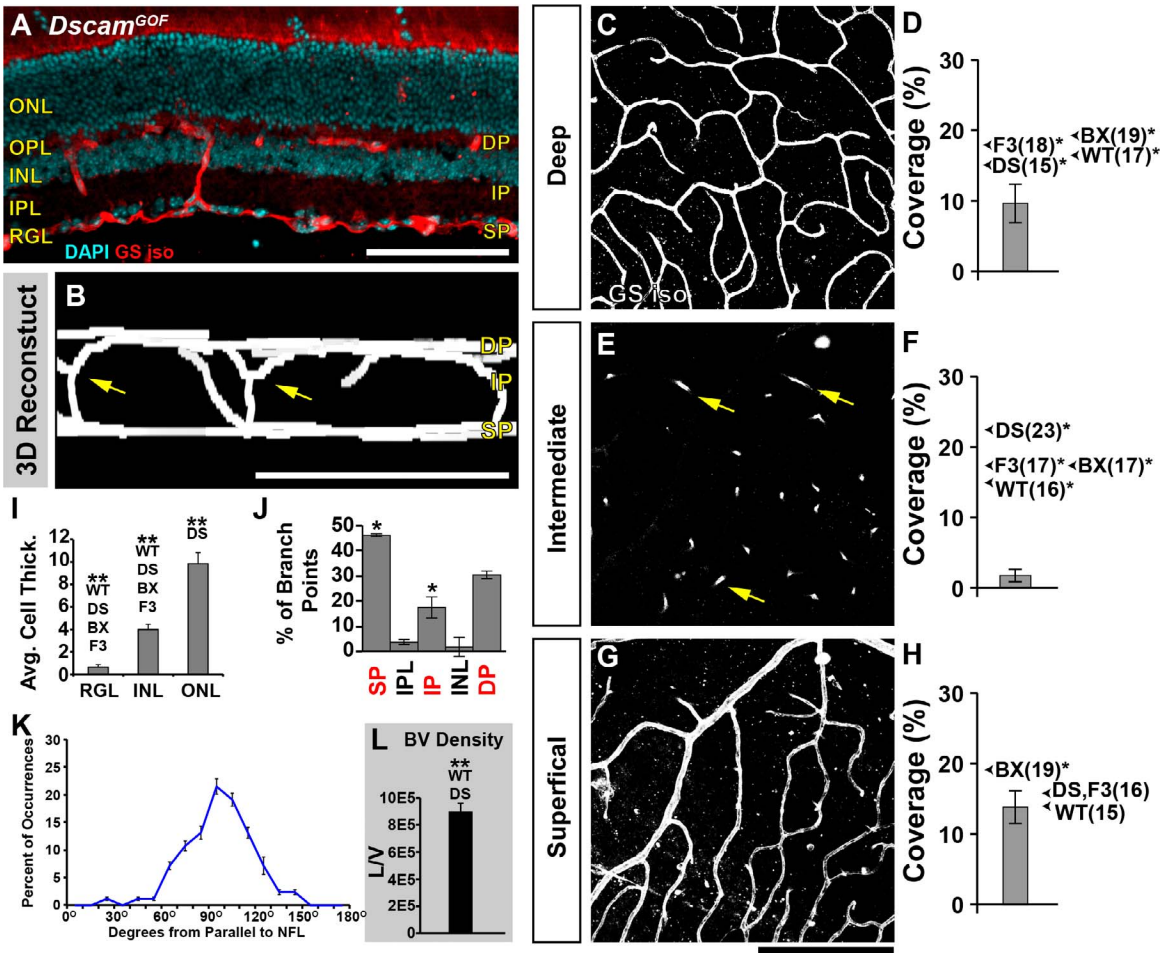

Figure 5. Analysis of retinal vasculature in the *Dscam*^{GOF} retina. Retinal vasculature was analyzed in retinas overexpressing *Dscam*, *Dscam*^{GOF}, retinas at P28. These retinas have significantly reduced number of neurons within the inner retina due to an increase in developmental cell death, while maintaining lamination within the inner retina. (**A**) Cross section of retina stained with GS isolectin and DAPI. (**B**) Digital reconstruction of vessel image in whole mount flipped to view the *x*/*z*-axis. Note the lacking IP (*yellow arrows*). (**C**, **D**) Analysis of the DP. A significant decrease in coverage was detected compared with all other genotypes. *Arrows* show the average coverage of other genotypes for comparison and the average value is denoted within *parentheses*. *Denotes statistical differences. (**E**, **F**) Analysis of the IP. *Dscam*^{GOF} retinas lack an IP. Vessel branching was observed at the boundary of the INL and IPL (*yellow arrows*), yet these vessels never ramified to create an IP. (**G**, **H**) Analysis of SP. A significant decrease in coverage was detected compared to the *Bax*$^{-/-}$ retina. (**I**) Cellular thickness of each cellular layer. There were statistically fewer cells within the RGL and INL compared with all strains. There were statistically more cells within the ONL compared with *Dscam*$^{-/-}$. (**J**) Analysis of interplexus vessel branching. A statistical increase in the frequency of BPs within the RGL and a statistical decrease at the IP was observed when comparing to *WT*. (**L**) Density of *Dscam*^{GOF} vessels. A significant increase in vessels was detected when compared to *WT* and *Dscam*$^{-/-}$ retinas. *Error bars*: SD. One-way ANOVAs were used to statistically compare *Dscam*^{GOF} with all other strains for cell thickness, plexi coverage, and vessel density (*P* values are included in other figures). Tukey's pairwise comparison was used to compare each group. Student's *t*-test was used to statically compare BPs to *WT*. *$P \leq 0.05$. Mann-Whitney *U* test was used to statistically compare *Dscam*^{GOF} versus all other strains. BX, *Bax*$^{-/-}$; DS, *Dscam*$^{-/-}$; F3, *Fat3*$^{-/-}$; W, *WT*. *Scale bars*: (**A**, **B**) 100 μm, (**G**) 200 μm.

the retinal laminae (Fig. 4G). A significant increase in BPs was detected within the INL of *Fat3*$^{-/-}$ retinas, 93% of these falling within the OMPL (Fig. 4G).

After observing defects in the formation of IP in *Dscam*$^{-/-}$ retinas, we decided to analyze the retinal vasculature within mice that overexpress *Dscam* (*Dscam*^{GOF}) at P28 (Fig. 5). In *Dscam*^{GOF} retinas, the ectopic and overexpression of *Dscam* results in a significantly thinner retina compared with all other strains (Figs. 5A, 5I).[25] *Dscam*^{GOF} retinas maintained formation of the DP and SP (Figs. 5B, 5C, 5G), although the coverage of the DP was significantly reduced compared with all strains, and coverage of the SP was significantly reduced compared with *Bax*$^{-/-}$ (Figs. 5D, 5H). Interestingly, *Dscam*^{GOF} retinas lacked an IP (Figs. 5B, 5E), even though vessels continued to branch at the neuron-neurite interface between the INL and IPL (Figs. 5B, 5E, arrows). The orientation of interplexus connections ran perpendicular to the plexi and continued to branch at areas spatially correlated to where the three plexi should form (Figs. 5J, 5K).

Taken together, these data provide evidence that displacement of neurons in the IPL of the *Dscam*$^{-/-}$ and *Bax*$^{-/-}$ retinas result in misprojection of vessels through the IPL. Moreover, the presence of an ectopic plexus lamina in the *Fat3*$^{-/-}$ retina and branching of vessels in the *Dscam*^{GOF} at the INL/IPL junction, implicate the neuron-neurite interface as a point of vessel branching.

Having characterized the organization of the retinal vessels in *Bax*, *Dscam*, and *Fat3* mutant retinas, we next set out to determine if disorganization of cell types associated with vascular development could explain these results.

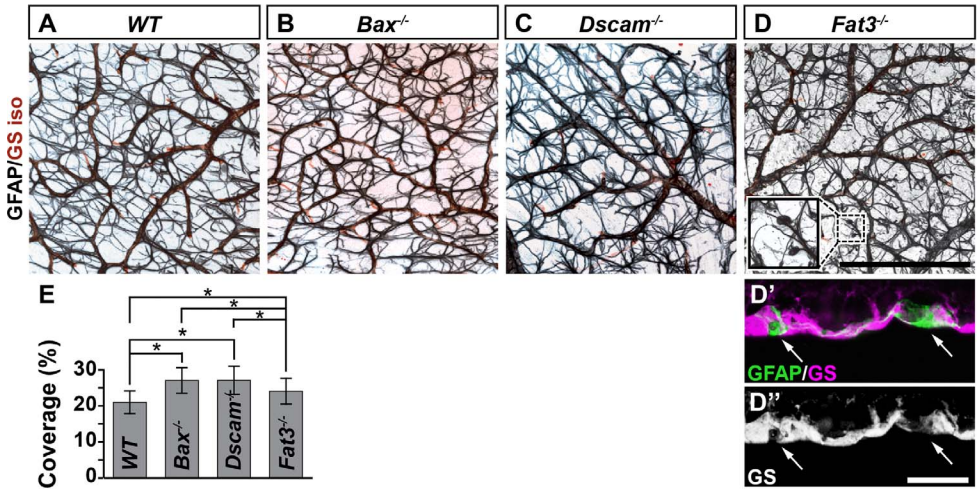

Figure 6. Astrocytes in mutant strains. (**A–D**) Postnatal day 28 whole retinas stained with GFAP and GS isolectin. The characteristic star-shaped morphology of astrocytes was present in all of the models and their processes wrapped blood vessels. Within *Fat3*$^{-/-}$ retinas, globe-shaped processes were found at some tips of astrocytes and filled areas of the inner limiting membrane that were discontinuous (*arrows* in **D'** and **D''**). (**E**) Graph illustrating the coverage of GFAP within whole retinas. A significant increase in coverage was detected when comparing all of the strains to *WT*. A significant decrease in coverage was detected when comparing *Fat3*$^{-/-}$ to *Bax*$^{-/-}$ or *Dscam*$^{-/-}$ mice. $n \geq 3$ mice was used for each strain. *Error bars*: SD. A 1-way ANOVA was used to statistically analyze the data ($P \leq 2.69 \times 10^{-13}$). Tukey's pairwise comparison was used to compare between groups. *Denotes statistical differences. *Scale bars*: (**D**) 200 μm, (**D''**) 20 μm. (**D**, *inset*), 44 × 44 μm.

Astrocytes

Whole retinas were stained with GFAP to visualize the morphology and density of astrocytes at P28 (Fig. 6).[35] Astrocytes were morphologically normal within *Bax*$^{-/-}$ and *Dscam*$^{-/-}$ retinas (Figs. 6A–C), whereas astrocytes within *Fat3*$^{-/-}$ retinas contained globe-shaped projections at some of their tips (Fig. 6D) that filled in areas where the inner limiting membrane was discontinuous (Figs. 6D', 6D''). Astrocytes continued to wrap vessels in all genotypes. The coverage of astrocytes was determined through confocal microscope images of GFAP staining within the NFL and RGL. A correlation between neural densities within the RGL of our genetic models (Fig. 2E) and their corresponding astrocyte coverage (Fig. 6E) was found, consistent with previous studies.[36–38]

Müller Cells

The density and morphology of MCs was assayed by staining sections of retina with GS and vimentin at P28 (Fig. 7).[39,40] No significant differences in the density of MCs or the trajectory at which MC radial processes project was detected when comparing all models (Figs. 7Q, 7R). When assaying the morphology of the tangential processes, we discovered that these processes were confined to neurite-containing laminae in all genotypes (Figs. 7M–P). This is most apparent in the IPL of *Dscam*$^{-/-}$ retinas, where MC processes were observed abutting but not invading the INL or RGL (Figs. 7G, 7O), and was further corroborated in the *Fat3*$^{-/-}$ retina where tangential processes were found within the OMPL (Figs. 7H, 7P). In MCs of *Bax*$^{-/-}$, *Dscam*$^{-/-}$, *Fat3*$^{-/-}$ retinas, GFAP was detected and confirmed with vimentin staining (Figs. 7M–O and not shown).

Microglia

To assay microglia organization, P28 retinas were stained with IBA-1 (Fig. 8).[41] Microglia are located within neurite-containing laminae of the retina: the OPL, IPL, and the OMPL of *Fat3*$^{-/-}$ retinas (Figs. 8A–D). Significant increases in microglia density compared with *WT* were found in all strains, except within the IPL when comparing *WT* with *Fat3*$^{-/-}$ (Figs. 8I, 8N).

Neurons

Next, we tested whether the displaced neurons within the IPL of *Dscam*$^{-/-}$ retinas correlated with misdirection of vessels and if this interaction was attractive or repulsive. To test this, whole *Dscam*$^{-/-}$ retinas were stained with GS isolectin, DRAQ5, and IBA-1 and then imaged with a confocal microscope at P14, a time point when intermediate vessels are forming[1] and slightly before intraretinal bleeding was observed in *Dscam* mutants (Figs. 9A, 9C). We then mapped vessels spanning the IPL and the location of displaced neurons and microglia (Figs. 9B, 9D–F). The distance between vessels and the nearest displaced neuron or microglia was measured and plotted compared with a control in which the vessels were flipped along the horizontal axis (Figs. 9G, 9H) (see Materials and Methods). Both neurons and microglia were statistically closer to vessels than the flipped controls, suggesting that neural somata and/or microglia are attracting vessel growth (Fig. 9H). Microglia were statistically closer to vessels than neural somas in both the peripheral and central retina (Fig. 9H).

Neuron Placement Affects the Expression Patterns of Angiogenic Factors

We next wanted to test whether the displacement of neurons within the inner retinas of *Dscam*$^{-/-}$ mice could alter the expression patterns of angiogenic factors, which could in turn explain vascular defects within the inner retina. In situ hybridization was performed on *Dscam*$^{-/-}$ retinas and littermate controls at P14 to visualize expression patterns of four angiogenic factors that are critical during retinal angiogenesis: *Vegfa*,[1,5,6,13,19,42] *Vegfr2* (KDR/Flk-1),[8] *Sema3C*,[43] and *Sema3E*[9,44] (Fig. 10).

In *WT* and *Dscam*$^{-/-}$ retinas, *Vegfa* was highly expressed by cells within the middle of the INL, likely MCs, consistent with a previous study.[13] Expression of *Vegfa* was also observed to a lesser extent within most neurons of the INL and RGL (Figs.

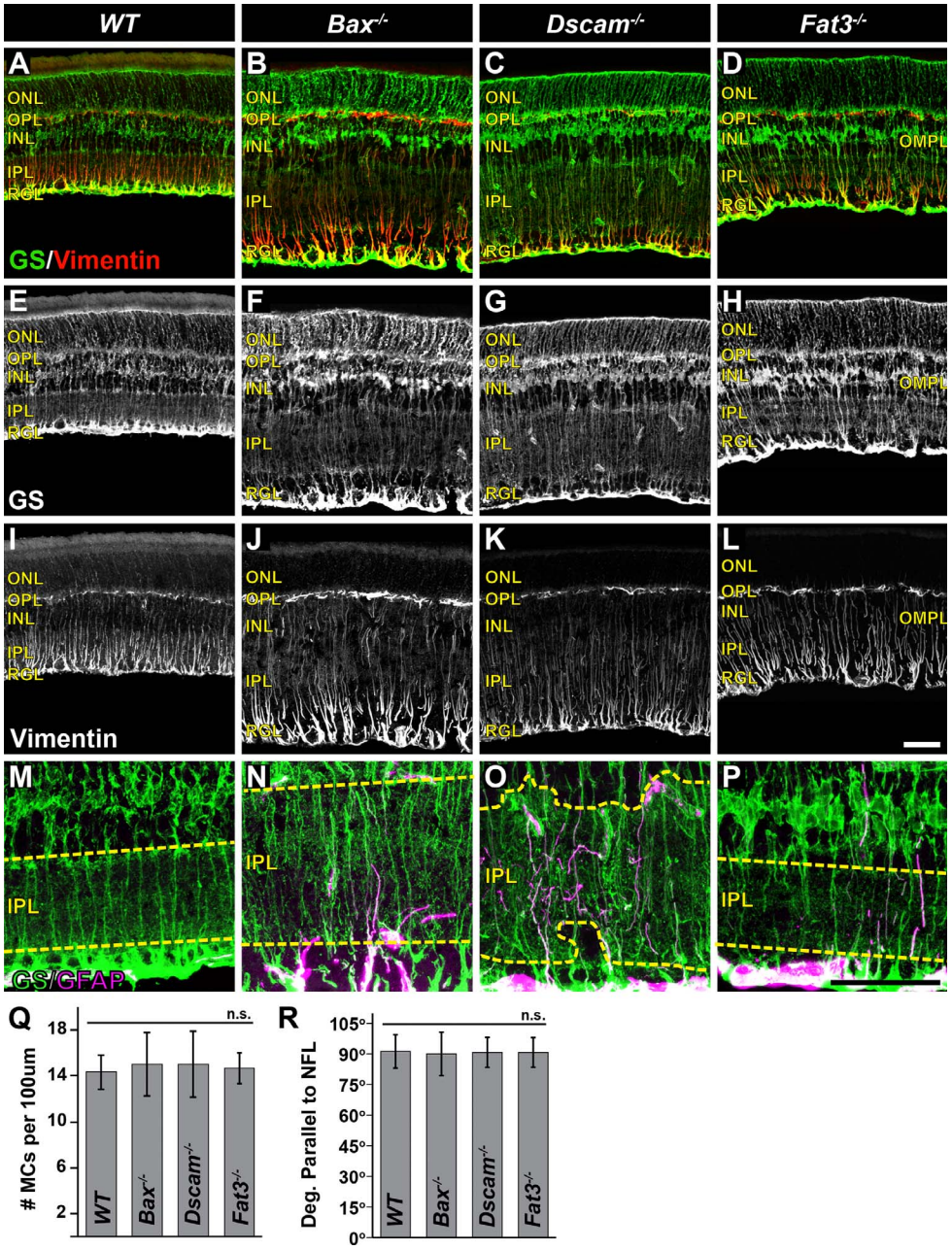

Figure 7. Müller cells in mutant strains. (**A–L**) Postnatal day 28 retina sections stained with GS and vimentin. (**M–P**) High-magnification images of GS and GFAP staining within the IPL. *Yellow dashed line* outlines the boundary of the IPL. (**Q**) *Graph* illustrating MC density. No significant difference in cell number was detected. (**R**) *Graph* illustrating measurement of MC radial process projections. $n \geq 3$ mice was used for each strain per quantification. *Error bars*: SD. A 1-way ANOVA was used to statistically analyze the data separately (MC density: $P = 0.88$; MC radial process: $P = 0.27$). *Scale bars*: (**L**, **P**) 50 μm.

10A, 10B), and in displaced neurons of *Dscam*$^{-/-}$ retinas (Fig. 10B, arrowheads). Expression of *Vegfr2* was also observed at high levels within cells central to the INL in the *WT* retina. This pattern was less distinct in *Dscam*$^{-/-}$ retinas. Expression of *Vegfr2* was found in most neurons of the INL and RGL in *WT* and *Dscam*$^{-/-}$ retinas (Figs. 10C, 10D), and again within displaced neurons of *Dscam*$^{-/-}$ retinas (Fig. 10D, arrowheads). Ectopic expression of *Vegfr2* was also detected within the INL of *Dscam*$^{-/-}$ retinas. Expression of *Sema3C* was observed throughout the retina (Figs. 10E, 10F), including displaced neurons in the *Dscam*$^{-/-}$ retina (Fig. 10F, arrowheads). Expression of *Sema3E* was observed in neurons in the RGL and to a lesser extent in the INL of both *WT* and *Dscam*$^{-/-}$ retinas (Figs. 10G, 10H), and within displaced neurons of *Dscam*$^{-/-}$ retinas (Fig. 10H, arrowheads). No staining was observed when probing retinas with mRNA sense probes (Supplementary Fig. S2).

Concentration Gradients of VEGF Are Influenced by Neuron Placement

The observations of altered expression patterns of *Vegfa* and *Vegfr2,* along with a recent study uncovering that VEGFR2 functions to titrate VEGF and prevent angiogenesis during early development,[8] brought us to ask the question, are VEGF concentration gradients altered in *Dscam* mutants? To test this,

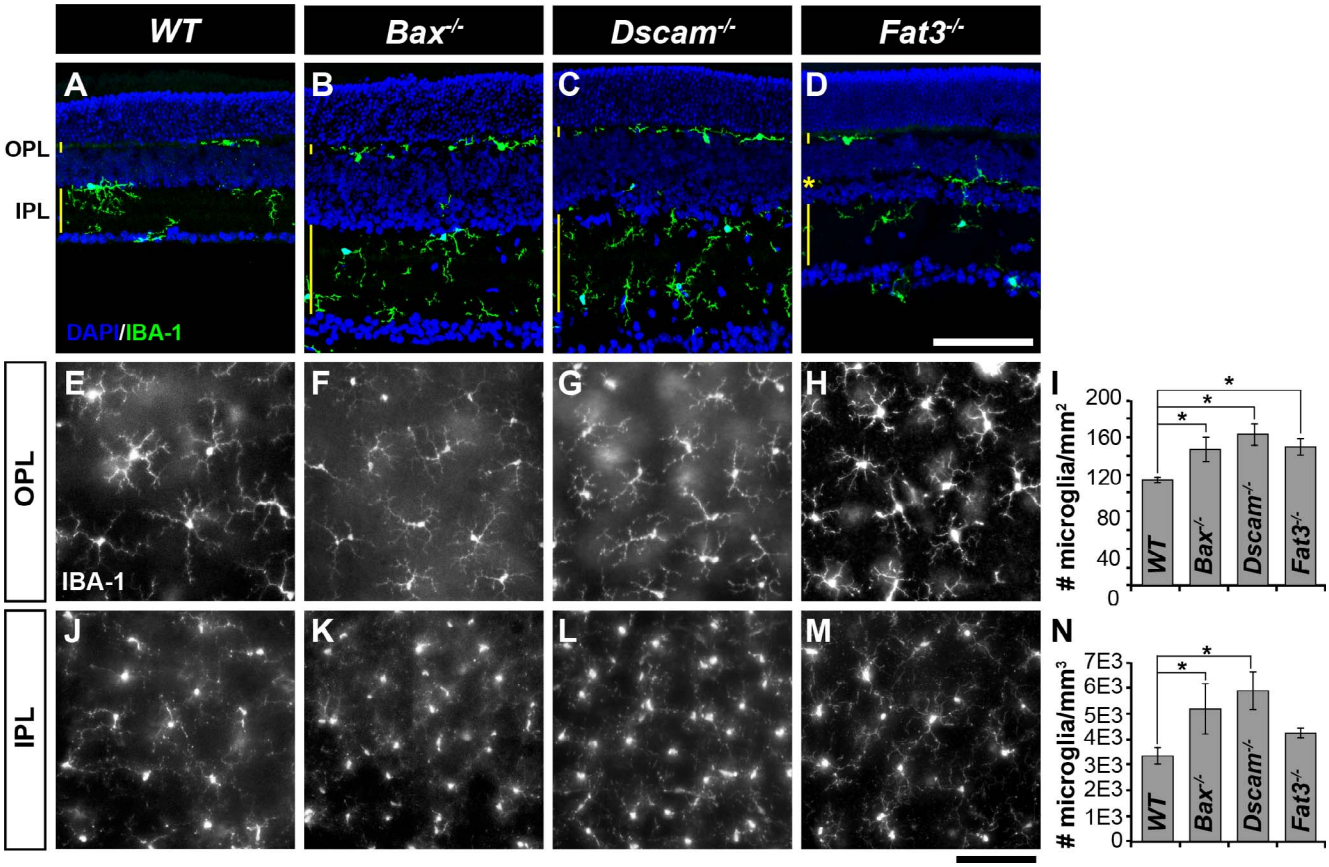

Figure 8. Microglia in mutant strains. (**A–D**) Postnatal day 28 retina sections stained with IBA-1 and DAPI. Microglia were found within neurite-containing laminae of retina: the OPL, IPL, and the OMPL of *Fat3*$^{-/-}$mice. (**E–H**) Microglia within the OPL in whole retinas. (**I**) *Graph* illustrating density of microglia within the OPL. (**J–M**) Microglia within the IPL in whole retinas. (**N**) *Graph* illustrating density of microglia within the IPL. Within the OPL, a significant increase in microglia was observed in all models, when compared with *WT*. Within the IPL, a significant increase in microglia was observed in *Bax*$^{-/-}$ and *Dscam*$^{-/-}$ when compared with *WT*. $n \geq 3$ mice was used for each strain per quantification. *Error bars*: SD. A 1-way ANOVA was used to statistically analyze the data (OPL: $P \leq 1.80 \times 10^{-3}$; IPL: $P \leq 6.02 \times 10^{-3}$). Tukey's pairwise comparison was used to compare between groups. *Denotes statistical differences. *Scale bars*: (**D**, **M**) 100 μm.

immunohistochemistry was performed to visualize the distribution of VEGF protein throughout *Dscam*$^{-/-}$ retinas and littermate controls at P14 (Fig. 11). In *WT* and *Dscam*$^{-/-}$ retinas, diffuse VEGF staining was observed throughout the entire retina excluding the ONL (Figs. 11A, 11B'). More intense VEGF immunoreactivity was observed on the surface of cell bodies, including displaced cell bodies in *Dscam*$^{-/-}$ retinas, compared with the IPL neurites.

To identify which type of cells within the IPL were accumulating more VEGF relative to the neurites, P14 retina sections were stained with DRAQ5, VEGF, and PAX6, a marker for neurons.[45] Nuclei within the IPL of *WT* and *Dscam*$^{-/-}$ retinas were then quantified and sorted by makers for which they were positive (Fig. 11E). Our results indicate that all cell bodies accumulating VEGF on their surface were PAX6 positive, but not all PAX6-positive cells accumulated VEGF, suggesting that a subset of neurons regulate VEGF localization during IP formation. Western blot was performed to quantify the amount of VEGF protein within *Dscam*$^{-/-}$ retinas compared with *WT* littermates at P14. No significant differences in the amount of relative VEGF protein were detected (Fig. 11F).

Discussion

Retinal neovascularization and vascular patterning defects result in blinding retinal diseases. Changes in the neural retina in these diseases can initiate the growth of new vessels through the process of angiogenesis.[46] A better understanding of the basic principles regulating angiogenesis during development will help elucidate what is occurring during vascular proliferative diseases causing blindness.

In this study, we set out to address the origin of retinal bleeding in *Dscam* mutant mice. We find that abnormalities in neuron lamination in the inner retina can promote pathologic angiogenesis, disrupting neural lamination leads to significant patterning changes in blood vessels, the neuron-neurite interface is a point of vessel branching, the displacement of neurons and microglia correlates with an attractive misdirection of growing vessels, and the displacement of neurons is sufficient to alter the expression and localization of angiogenic factors.

Neuron Disorganization and Retinal Angiogenesis

Developmental retinal lamination defects and vascular abnormalities are observed in heritable retinal dystrophies, such as retinitis pigmentosa (RP) and Leber congenital amaurosis (LCA) and are caused by mutations in the *Crumbs homologue 1* (*CRB1*) gene,[22] which is required for retinal lamination structuring within both human and mouse outer retinas.[22] In humans, the loss of *CRB1* is associated with retinal lamination defects within LCA patients,[47] and vascular abnormalities leading to edema and retinal detachment within RP patients.[48]

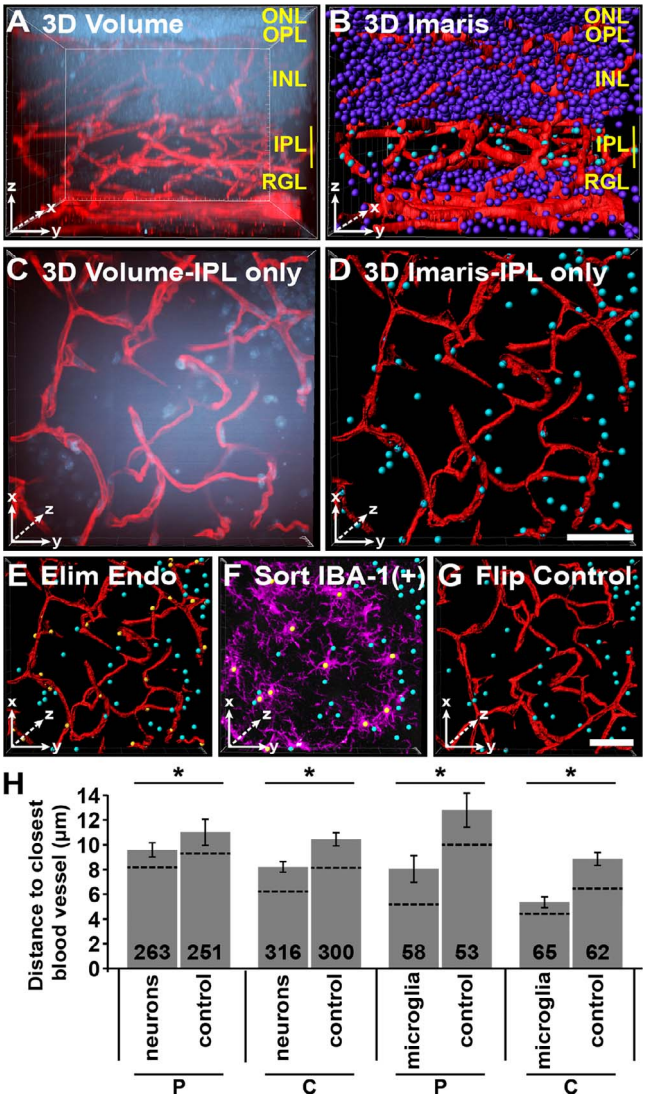

Figure 9. Nuclei to nearest vessel three-dimensional (3D) assay. Using Bitplane's Imaris, we developed a 3D assay to measure the neural soma and microglia to the nearest vessel. This was performed on *Dscam*$^{-/-}$ retinas at P14 due to the large number of displace neurons within the IPL. (**A**) A 3D rendering of image of whole retina stained with DRAQ5 and GS isolectin. (**B**) Blood vessels were made into surfaces (*red*) while nuclei were made into spots (*purple* and *cyan*). Spots within the IPL are selected and colored *cyan*, while all other nuclei are *purple*. (**C**) Cropped view of IPL 3D rendering. Flipped to view the *x*/*y*-axis. (**D**) Cropped view of IPL of Imaris objects. Note that some nuclei in (**C**) are not present in (**D**). This is because they are part of the INL not the IPL and were excluded from analysis. (**E**) Endothelial nuclei were sorted by vessel reconstruction and GS isolectin staining and eliminated from analysis. (**F**) Microglia were sorted by IBA-1 staining (*purple*). (**G**) Vessels were flipped along the horizontal axis and served as an internal control. This control randomized the distribution of nuclei allowing for the comparison between the relative placement of cells to blood vessels to that of random distribution. (**H**) *Graph* illustrating the average distance between neurons and vessels or microglia and vessels. Number in *bar* is the total number of spots quantified. *Dotted line* represents the median. Images were captured from six different retinas. *Error bars*: SE. Student's *t*-test was used to analyze data. $^{*}P \leq 0.05$. *Scale bars*: (**D**, **G**) 25 µm.

In *CRB1* mutant mouse models, structural alterations in the outer limiting membrane (OLM) result in the restructuring of the outer retina in the formation of pseudorosettes and retinal folding.[49,50] Similarly, we identify that developmental alterations in neural lamination within inner portions of *Dscam*$^{-/-}$ retinas cause abnormalities in the patterning and integrity of vessels as they develop. Taken together, these observations suggest that developmental, disease, and age-related changes in neural lamination could promote abnormal vascular growth and retinal bleeding.

Neuron Disorganization Mislocalizes Angiogenic Factors

In the mouse, retinal vessels form via a process of angiogenesis and their growth is guided by secreted molecules that act to attract or repel growing blood vessels.[51] A growing body of literature has begun to uncover that angiogenesis is regulated by similar molecules and mechanisms to that of the nervous system, and that the vascular and nervous systems often engage in cross-talk during development and disease.[51] Therefore, regulating the balance and expression of these shared factors is important for proper development and maintenance of these systems. Moreover, the highly organized retina serves as an ideal model for understanding these principles.

Vascular endothelial growth factor is a key regulator of angiogenesis.[52] Within the retina, VEGF is required for the initiation of angiogenic sprouts, arteriole versus venous fate determination, and vessel stabilization.[1,13,19,42] During the initial development of the superficial vessels, neurons have been shown to regulate VEGF activity through VEGFR2-induced engulfment of VEGF, preventing immature vessels from sprouting into the retina.[8] As development proceeds, neural-derived VEGF has been shown to regulate the formation of the intraretinal vessels.[5,6] These studies begin to illustrate the importance of neural regulation on VEGF bioavailability and how this regulation changes over time, presumably to aid with vessel patterning.

Our results implicate an additional requirement to this regulation; that is, the placement of neurons. During development of the IP in *WT* retinas, we observed accumulation of VEGF on the surface of neural somas abutting the INL. In other model systems, a capture and presentation mechanism has been well documented, such as netrins for axon guidance in *Drosophila*,[53,54] UNC-6 for axon guidance and dendrite repulsion in *Caenorhabditis elegans,*[55,56] and F-spondin for axon guidance in chicks,[57] where a diffusible guidance molecule is captured and presented to growth cones allowing multicellular organisms to tightly regulate the growth of axons and dendrites. Perhaps formation of the IP in the retina uses a similar mechanism, where neurons abutting the IPL accumulate MCs and neural-derived VEGF and present it to vessel growth cones promoting vessel branching and ramification at the neuron-neurite interface. In *Dscam* mutants, we find the displacement of neurons is sufficient to mislocalize the distribution of VEGF and that the cell surface accumulation of VEGF is largely absent in the INL and abundant in displaced neurons throughout the IPL.

Semaphorins are a class of repelling guidance molecules originally found to be important for nervous system development and have recently been shown to be important for angiogenesis.[51] During blood vessel growth, secreted semaphorins modulate delta-like 4 (Dll4)-notch signaling, disrupting tip/stalk cell determination and causing cytoskeletal destabilization, preventing the growth of vessels in a particular direction or altogether.[58] In our study, we analyzed the expression patterns of two secreted semaphorins known to be important for angiogenesis in the retina, *Sema3C*[43] and *Sema3E*.[9,44] We find that both of these are highly expressed normally in the retina and that these are almost always expressed by displaced cells in *Dscam* mutants.

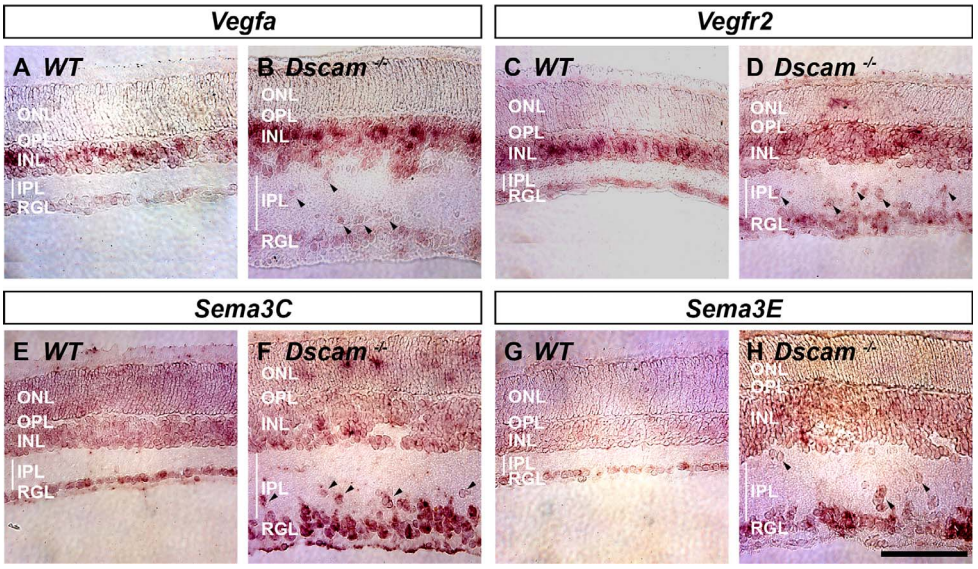

Figure 10. Neuron placement affects the expression patterns of angiogenic factors. Retinas were prepared for in situ hybridization at P14 comparing *Dscam*$^{-/-}$ to littermate controls. (**A**, **B**) *Vegfa* expression was detected strongly within the central INL of *WT* and *Dscam*$^{-/-}$ retinas and to a lesser extent within most cells of the INL and RGL. *Vegfa* was also detected within displaced neurons in *Dscam*$^{-/-}$ retinas (*arrowheads*). (**C**, **D**) *Vegfr2* expression was detected strongly within the central INL of *WT* retinas and to a lesser extent in cells throughout the INL and RGL. *Vegfr2* expression was detected within the INL and RGL of *Dscam*$^{-/-}$ retinas although the central expression in the INL was less distinct. *Vegfr2* expression was also detected in patches in the ONL and within displaced neurons of *Dscam*$^{-/-}$ retinas (*arrowheads*). (**E**, **F**) *Sema3C* expression was detected throughout all cellular layers in *WT* and *Dscam*$^{-/-}$ retinas, including displaced neurons in *Dscam*$^{-/-}$ retinas (*arrowheads*) (**G**, **H**) *Sema3E* expression was detected within the RGL and to a lesser extent in the INL of *WT* and *Dscam*$^{-/-}$ retinas, and within displaced neurons of *Dscam*$^{-/-}$ retinas (*arrowheads*). $n = 4$ retinas from two mice were analyzed. *Scale bar*: (**H**) 100 μm.

A possible model to explain the disorganization of intraretinal vessels in *Dscam* mutants is that the displacement of neurons leads to lack of a distinct VEGF cue that normally promotes vessel branching and ramification and is exacerbated by the misexpression of repulsive semaphorin cues leading to vascular defects and retinal bleeding. Future studies targeting VEGF, VEGF receptors, and semaphorins will be performed to test this hypothesis.

Glia and the Retinal Vasculature

The retina contains three types of glia that are intimately linked to the retinal vasculature: astrocytes, MCs, and microglia. Interactions between these cells, along with neurons and cells of the vasculature, are required to form the neurovascular unit. Associated changes in neurons and glia have been reported in pathologic conditions of the retina; however, a cause-and-effect relationship is yet to be resolved.[59] In this study, we observe changes in the organization of these populations in mutant strains with abnormal neural organization within the inner retina, suggesting a role for neurons in initiating and maintaining these cellular interactions.

Astrocytes were the least-affected glia population in our mutant strains. We found a correlation between neural densities within the RGL and astrocyte densities, consistent with previous reports demonstrating that platelet-derived growth factor (PDGF) released by neurons promotes astrocyte growth[36,37] and that depletion of retinal ganglion cells results in decreased astrocyte populations.[38] Astrocyte gross morphology appeared to be unaffected by neuron organization because astrocytes were found within the NFL of all our mutant stains and their processes wrapped superficial vessels. It can be reasoned that the globe-shaped projections at the tips of *Fat3*$^{-/-}$ astrocytes follow misprojected neurites from neurons forming the IMPL. However, these changes were not reflected by the retinal vessels.

During development, hypoxia drives the expression and release of VEGF from MCs and it is thought the MCs provide structural support for the migration of endothelial cells during vessel formation.[1,13] Mature MC tangential processes wrap retinal vessels to help form the BRB.[11] Selective ablation of MCs in the adult retina leads to severe changes in the organization of retinal vessels, breakdown of the BRB, and eventually intraretinal neovascularization.[60] We found that the radial processes of MCs were unaffected by neural lamination, whereas the tangential processes were redirected toward ectopic neurites. However, no considerable changes were observed in MCs that could describe vascular defects.

We also identified changes to microglia organization in our mutant stains. We found that microglia limit themselves to the neurite-containing laminae within the retina and frequently find them at the neuron-neurite interface. Microglia are known to regulate the branching of developing superficial vessels.[16] A potential model to explain the branching pattern observed at the neuron-neurite interface in this study is that microglia position themselves at the neuron-neurite interface and promote branching of vessels at this interface. Microglia depletion studies aimed at differentiating these possibilities will be performed in future studies to address this question.

Conclusions

This study demonstrates the importance of neuronal placement during intraretinal vessel development. Our current working model is that lamination defects cause mispresentation of neural-derived factors organizing vascular growth leading to the disorganization of retinal vessels (Fig. 12). Whether the changes in neural lamination are directly causing changes in vessel development, are secondary to neural-driven glial changes, or both remain to be elucidated and are the focus of future experiments.

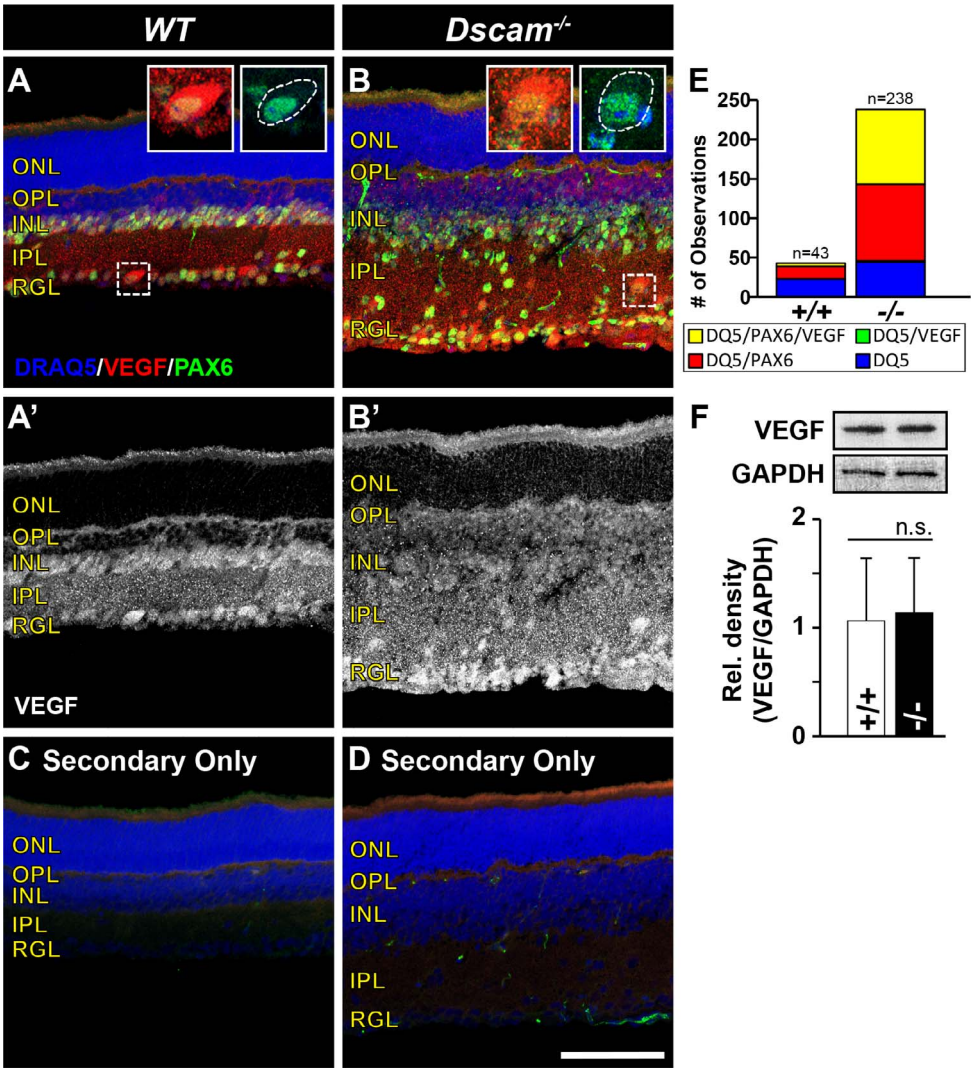

Figure 11. Vascular endothelial growth factor localization is influenced by neural placement. Retinas were prepared for immunohistochemistry at P14 comparing *Dscam*$^{-/-}$ with littermate controls. (**A**, **B**) Retina sections stained with DRAQ5, VEGF, and PAX6. *Insets* illustrate the accumulation of VEGF on the surface of neurons. *White dotted line* in the *second inset* shows the outline of neuron soma. (**A'–B'**) Vascular endothelial growth factor channel split out for better visualization. (**C**, **D**) Control retinas stained with secondary antibodies only. Staining of VEGF and PAX6 is absent. α-Mouse staining can be seen in blood vessels. (**E**) *Graph* illustrating the raw cell counts of nuclei within the IPL of *WT* and *Dscam*$^{-/-}$ retinas. Nuclei were sorted into four bins (*yellow* = DRAQ5/PAX6/VEGF; *green* = DRAQ5/VEGF; *red* = DRAQ5/PAX6; *blue* = DRAQ5). All cells VEGF+ were PAX6+, but not all PAX6+ cells were VEGF+. (**F**) Western blot was performed to quantify the total amount of VEGF protein in *Dscam*$^{-/-}$ retinas compared with littermate controls. No significant difference was detected when comparing the relative density (VEGF/GAPDH) of VEGF protein in *Dscam*$^{-/-}$ and *WT* littermate controls. *Error bars*: SD. Student's *t*-test was used to analyze data ($P = 0.83$). $n \geq 3$ mice was used for each strain per quantification. DQ5, DRAQ5. *Scale bar*: (**D**) 100 μm. (**A**, **B** *inset*), 31 × 31 μm.

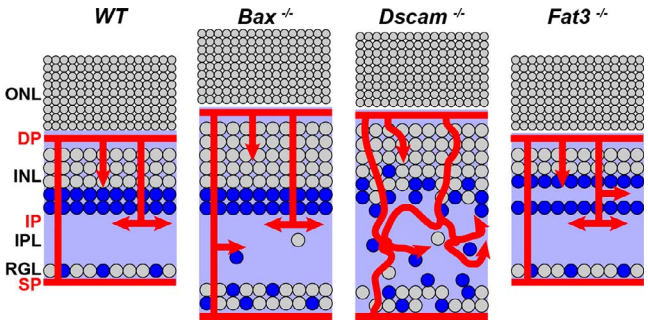

Figure 12. Working model. Disrupting the organization of the neurons in the inner retina in turn changes how neural-derived factors are presented altering the organization of non-neural components. Illustrated here is VEGF distribution to serve as an example. There are likely many neural-derived angiogenic factors influenced by neuron placement.

Acknowledgments

The authors thank Ann Norton, the director of the optical imaging core at the University of Idaho, for her support and training with imaging and Bitplane's Imaris. The authors also thank Joshua Sukeena and Carlos Galicia for their help with in situ hybridization.

Supported by National Eye Institute Grant EY020857 (PGF) and EY021146 (MRD). Imaging support was provided by National Institutes of Health Grants P20 RR016454 (PGF), P30 GM103324-01 (PGF), and P20 GM103408 (PGF).

Disclosure: **A.B. Simmons**, None; **M.M. Merrill**, None; **J.C. Reed**, None; **M.R. Deans**, None; **M.M. Edwards**, None; **P.G. Fuerst**, None

References

1. Fruttiger M. Development of the retinal vasculature. *Angiogenesis*. 2007;10:77–88.
2. Mehta S. Age-related macular degeneration. *Prim Care*. 2015; 42:377–391.
3. Hellstrom A, Smith LE, Dammann O. Retinopathy of prematurity. *Lancet*. 2013;382:1445–1457.
4. Lutty GA. Effects of diabetes on the eye. *Invest Ophthalmol Vis Sci*. 2013;54:ORSF81-87.
5. Kurihara T, Westenskow PD, Bravo S, Aguilar E, Friedlander M. Targeted deletion of Vegfa in adult mice induces vision loss. *J Clin Invest*. 2012;122:4213–4217.
6. Usui Y, Westenskow PD, Kurihara T, et al. Neurovascular crosstalk between interneurons and capillaries is required for vision. *J Clin Invest*. 2015;125:2335–2346.
7. Luo L, Uehara H, Zhang X, et al. Photoreceptor avascular privilege is shielded by soluble VEGF receptor-1. *eLife*. 2013;2: e00324.
8. Okabe K, Kobayashi S, Yamada T, et al. Neurons limit angiogenesis by titrating VEGF in retina. *Cell*. 2014;159:584–596.
9. Kim J, Oh WJ, Gaiano N, Yoshida Y, Gu C. Semaphorin 3E-Plexin-D1 signaling regulates VEGF function in developmental angiogenesis via a feedback mechanism. *Genes Dev*. 2011;25: 1399–1411.
10. Buehler A, Sitaras N, Favret S, et al. Semaphorin 3F forms an anti-angiogenic barrier in outer retina. *FEBS Lett*. 2013;587: 1650–1655.
11. Vecino E, Rodriguez FD, Ruzafa N, Pereiro X, Sharma SC. Glia-neuron interactions in the mammalian retina. *Prog Retin Eye Res*. 2015;51:1–40.
12. Agathocleous M, Harris WA. From progenitors to differentiated cells in the vertebrate retina. *Annu Rev Cell Dev Biol*. 2009; 25:45–69.
13. Stone J, Itin A, Alon T, et al. Development of retinal vasculature is mediated by hypoxia-induced vascular endothelial growth factor (VEGF) expression by neuroglia. *J Neurosci*. 1995;15: 4738–4747.
14. Kolb H. Glial cells of the retina. In: Kolb H, Fernandez E, Nelson R, eds. *Webvision: The Organization of the Retina and Visual System*. Salt Lake City, UT: University of Utah Health Sciences Center; 1995.
15. Watanabe T, Raff MC. Retinal astrocytes are immigrants from the optic nerve. *Nature*. 1988;332:834–837.
16. Arnold T, Betsholtz C. Correction: the importance of microglia in the development of the vasculature in the central nervous system. *Vasc Cell*. 2013;5:12.
17. Dorrell MI, Aguilar E, Friedlander M. Retinal vascular development is mediated by endothelial filopodia, a preexisting astrocytic template and specific R-cadherin adhesion. *Invest Ophthalmol Vis Sci*. 2002;43:3500–3510.
18. Gnanaguru G, Bachay G, Biswas S, Pinzon-Duarte G, Hunter DD, Brunken WJ. Laminins containing the beta2 and gamma3 chains regulate astrocyte migration and angiogenesis in the retina. *Development*. 2013;140:2050–2060.
19. Scott A, Powner MB, Gandhi P, et al. Astrocyte-derived vascular endothelial growth factor stabilizes vessels in the developing retinal vasculature. *PLoS One*. 2010;5:e11863.
20. Sanes JR, Zipursky SL. Design principles of insect and vertebrate visual systems. *Neuron*. 2010;66:15–36.
21. Masland RH. The neuronal organization of the retina. *Neuron*. 2012;76:266–280.
22. Richard M, Roepman R, Aartsen WM, et al. Towards understanding CRUMBS function in retinal dystrophies. *Hum Mol Genet*. 2006;15:R235–R243.
23. Fuerst PG, Harris BS, Johnson KR, Burgess RW. A novel null allele of mouse DSCAM survives to adulthood on an inbred C3H background with reduced phenotypic variability. *Genesis*. 2010;48:578–584.
24. Fuerst PG, Bruce F, Rounds RP, Erskine L, Burgess RW. Cell autonomy of DSCAM function in retinal development. *Dev Biol*. 2012;361:326–337.
25. Li S, Sukeena JM, Simmons AB, et al. DSCAM promotes refinement in the mouse retina through cell death and restriction of exploring dendrites. *J Neurosci*. 2015;35:5640–5654.
26. Deans MR, Krol A, Abraira VE, Copley CO, Tucker AF, Goodrich LV. Control of neuronal morphology by the atypical cadherin Fat3. *Neuron*. 2011;71:820–832.
27. Longair MH, Baker DA, Armstrong JD. Simple neurite tracer: open source software for reconstruction, visualization and analysis of neuronal processes. *Bioinformatics*. 2011;27: 2453–2454.
28. Ramon y Cajal S. La rétine des vertébrés [in French]. *Cellule*. 1893;9:119–257.
29. Fuerst PG, Koizumi A, Masland RH, Burgess RW. Neurite arborization and mosaic spacing in the mouse retina require DSCAM. *Nature*. 2008;451:470–474.
30. Nelson SM, Frey RA, Wardwell SL, Stenkamp DL. The developmental sequence of gene expression within the rod photoreceptor lineage in embryonic zebrafish. *Dev Dyn*. 2008;237:2903–2917.
31. Stevens CB, Cameron DA, Stenkamp DL. Plasticity of photoreceptor-generating retinal progenitors revealed by prolonged retinoic acid exposure. *BMC Dev Biol*. 2011;11:51.
32. Xu Y, Ye H, Shen Y, et al. Dscam mutation leads to hydrocephalus and decreased motor function. *Protein Cell*. 2011;2:647–655.
33. de Andrade GB, Long SS, Fleming H, Li W, Fuerst PG. DSCAM localization and function at the mouse cone synapse. *J Comp Neurol*. 2014;522:2609–2633.
34. Harder JM, Libby RT. BBC3 (PUMA) regulates developmental apoptosis but not axonal injury induced death in the retina. *Mol Neurodegener*. 2011;6:50.
35. Bignami A, Eng LF, Dahl D, Uyeda CT. Localization of the glial fibrillary acidic protein in astrocytes by immunofluorescence. *Brain Res*. 1972;43:429–435.
36. Fruttiger M, Calver AR, Kruger WH, et al. PDGF mediates a neuron-astrocyte interaction in the developing retina. *Neuron*. 1996;17:1117–1131.
37. Fruttiger M, Calver AR, Richardson WD. Platelet-derived growth factor is constitutively secreted from neuronal cell bodies but not from axons. *Curr Biol*. 2000;10:1283–1286.
38. Edwards MM, McLeod DS, Li R, et al. The deletion of Math5 disrupts retinal blood vessel and glial development in mice. *Exp Eye Res*. 2012;96:147–156.
39. Pixley SK, Kobayashi Y, de Vellis J. A monoclonal antibody against vimentin: characterization. *Brain Res*. 1984;317:185–199.
40. Haverkamp S, Wassle H. Immunocytochemical analysis of the mouse retina. *J Comp Neurol*. 2000;424:1–23.
41. Ito D, Imai Y, Ohsawa K, Nakajima K, Fukuuchi Y, Kohsaka S. Microglia-specific localisation of a novel calcium binding protein, Iba1. *Brain Res Mol Brain Res*. 1998;57:1–9.
42. Stalmans I, Ng YS, Rohan R, et al. Arteriolar and venular patterning in retinas of mice selectively expressing VEGF isoforms. *J Clin Invest*. 2002;109:327–336.
43. Yang WJ, Hu J, Uemura A, Tetzlaff F, Augustin HG, Fischer A. Semaphorin-3C signals through Neuropilin-1 and PlexinD1 receptors to inhibit pathological angiogenesis. *EMBO Mol Med*. 2015;7:1267–1284.

44. Fukushima Y, Okada M, Kataoka H, et al. Sema3E-PlexinD1 signaling selectively suppresses disoriented angiogenesis in ischemic retinopathy in mice. *J Clin Invest*. 2011;121:1974–1985.
45. Sebastian-Serrano A, Sandonis A, Cardozo M, Rodriguez-Tornos FM, Bovolenta P, Nieto M. Palphax6 expression in postmitotic neurons mediates the growth of axons in response to SFRP1. *PLoS One*. 2012;7:e31590.
46. Lieth E, Gardner TW, Barber AJ, Antonetti DA; Penn State Retina Research Group. Retinal neurodegeneration: early pathology in diabetes. *Clin Experiment Ophthalmol*. 2000; 28:3–8.
47. Jacobson SG, Cideciyan AV, Aleman TS, et al. Crumbs homolog 1 (CRB1) mutations result in a thick human retina with abnormal lamination. *Hum Mol Genet*. 2003;12:1073–1078.
48. den Hollander AI, Heckenlively JR, van den Born LI, et al. Leber congenital amaurosis and retinitis pigmentosa with Coats-like exudative vasculopathy are associated with mutations in the crumbs homologue 1 (CRB1) gene. *Am J Hum Genet*. 2001;69:198–203.
49. Mehalow AK, Kameya S, Smith RS, et al. CRB1 is essential for external limiting membrane integrity and photoreceptor morphogenesis in the mammalian retina. *Hum Mol Genet*. 2003;12:2179–2189.
50. van de Pavert SA, Kantardzhieva A, Malysheva A, et al. Crumbs homologue 1 is required for maintenance of photoreceptor cell polarization and adhesion during light exposure. *J Cell Sci*. 2004;117:4169–4177.
51. Carmeliet P. Blood vessels and nerves: common signals, pathways and diseases. *Nature Rev Genet*. 2003;4:710–720.
52. Carmeliet P, Ferreira V, Breier G, et al. Abnormal blood vessel development and lethality in embryos lacking a single VEGF allele. *Nature*. 1996;380:435–439.
53. Timofeev K, Joly W, Hadjieconomou D, Salecker I. Localized netrins act as positional cues to control layer-specific targeting of photoreceptor axons in *Drosophila*. *Neuron*. 2012;75:80–93.
54. Hiramoto M, Hiromi Y, Giniger E, Hotta Y. The *Drosophila* Netrin receptor Frazzled guides axons by controlling Netrin distribution. *Nature*. 2000;406:886–889.
55. Asakura T, Waga N, Ogura K, Goshima Y. Genes required for cellular UNC-6/netrin localization in *Caenorhabditis elegans*. *Genetics*. 2010;185:573–585.
56. Smith CJ, Watson JD, VanHoven MK, Colon-Ramos DA, Miller DM III. Netrin (UNC-6) mediates dendritic self-avoidance. *Nat Neurosci*. 2012;15:731–737.
57. Zisman S, Marom K, Avraham O, et al. Proteolysis and membrane capture of F-spondin generates combinatorial guidance cues from a single molecule. *J Cell Biol*. 2007;178: 1237–1249.
58. Gu C, Giraudo E. The role of semaphorins and their receptors in vascular development and cancer. *Exp Cell Res*. 2013;319: 1306–1316.
59. Coorey NJ, Shen W, Chung SH, Zhu L, Gillies MC. The role of glia in retinal vascular disease. *Clin Exp Optom*. 2012;95:266–281.
60. Shen W, Fruttiger M, Zhu L, et al. Conditional Mullercell ablation causes independent neuronal and vascular pathologies in a novel transgenic model. *J Neurosci*. 2012;32:15715–15727.